Dynamic Response Analysis of Pavement Structure of Steel-concrete Composite Beam Bridge under Triaxial Force of Tires

Baoxing Gong[1], Zhanyou Yan[1,*], Kaifan Xu[2] and Chunliu Li[3]

[1]College of Civil Engineering, Shijiazhuang Tiedao University, Shijiazhuang 050043, China
[2]Guangdong Zhonggong Architectural Design Institute Co. LTD, Guangzhou 510000, China
[3]Institute of Urban Construction, Hebei Normal University of Science & Technology, Qinhuangdao 066004, China

_____

Abstract

The dynamic stability and long-term safe operation of long span continuous beam bridge have potential safety hazards under the vehicle dynamic load. To reveal the dynamic response characteristics of the pavement structure of the steel-concrete composite three-span continuous beam bridge under the load of tires, a three-dimensional numerical model was established. The bridge deck irregularity was set for the vehicle model and the suspension force of rear axle was applied to the three span continuous beam bridge. The central difference method was used to solve the deflection, transverse and longitudinal stress of the pavement layer of the bridge deck, and the mechanical properties of the beam bridge under the vehicle loads were analyzed. Results show that the vertical deflection of the pavement layers of the steel-concrete three-span continuous beam bridge is 7.7% higher than that of the uniaxial force (vertical force) under the triaxial force of tire. The vertical deflection value of the pavement layers of the beam bridge is basically the same, while the vertical deflection at the bottom of the I-beam is 8.9% smaller than that of the pavement structure. The stress changes in the pavement structure of the bridge are mainly concentrated in the lower layer, and the longitudinal stress of the lower layer of the pavement structure and the I-beams both appear tension-compression alternation. The obtained conclusions in this study can provide the reference for the design and construction of similar steel-concrete composite long-span viaduct.

Keywords: Steel-concrete composite continuous beam, Pavement layers of bridge deck, Numerical analysis, Dynamic response

_____

1. Introduction

In recent decades, the urban viaduct, as an efficient, fast and effective way to alleviate traffic jams, has been widely applied in the world. However, with the rapid development of cities, urban traffic congestion is becoming increasingly serious, and some urban areas have to build long-span continuous beam bridges. Therefore, it is necessary to analyze the vehicle-bridge coupled vibration of the multi span continuous beam bridge under the traffic loads [1, 2].

With the increase of urban traffic flow, the vehicle load and driving speed have increased significantly. The moving vehicle load leads to the aggravation of vibration and damage of long-span continuous beam bridge, and even the bridge collapse accidents caused by vehicle overloading and overspeed are gradually increasing [3]. The vehicle-bridge coupled vibration has more and more influence on the bearing capacity and durability of bridges, which brings potential safety hazards for the daily operation of multi span continuous beam bridges.

Compared with ordinary highway, the multi span continuous beam bridge has large span, poor structural stability, and higher requirements for stability and deformation [4]. The vibration of the bridge caused by vehicle driving will increase the internal force of the structure and cause local fatigue damage of the components. Therefore, it is of important theoretical significance and engineering application value to study on the dynamic response and mechanical characteristics of the multi span

continuous beam bridge for the structural design and driving comfort of urban viaduct.

2. State of the art

At present, the research on vehicle-bridge dynamic coupling has always been a hot spot in the world, many scholars have carried out in-depth and detailed research and obtained a lot of results in vehicle-bridge coupling and bridge deck pavement. Suangga & Haripriambodo processed the bridge monitoring data by combining numerical analysis and linear regression, and they proposed a calculation method for the maximum deflection of three span continuous beam [5]. Mizrak & Esen established a rail vehicle bogie with 10 degrees of freedom and an Euler Bernoulli beam bridge model to evaluate the passenger comfort under moving load [6]. Based on the field monitoring and mechanical test data, Bayane et al. proposed a fatigue safety evaluation method for composite steel concrete viaducts, and verified its accuracy by indoor tests [7]. To quickly obtain the monitoring data of the steel-concrete composite railway viaduct after the earthquake, Narazaki et al. proposed an autonomous navigation method for unmanned aerial vehicles to automatically identify and quickly locate key structural components [8]. Aloisio et al. established a three-dimensional finite element numerical model of concrete 7-span continuous beam bridge to estimate concrete resistance, and then proposed an indirect method to estimate material properties from environmental vibration data [9].

With the increase of service time of the steel-concrete composite beam, the pavement structure of the steel-concrete composite beams appears a series of problems such as sliding, delamination, rutting and cracking, and some parts of the of the steel beam also appear cracks, fatigue and other diseases, which leads to the continuous increase of maintenance costs of steel-concrete composite beams and seriously damages the service life of steel-concrete composite beams [10]. According to the mechanical contact relationship between the vehicle and the bridge, Li & Xia established a three-dimensional vehicle-bridge coupling model, and they solved the dynamic response of each node of the bridge [11]. Based on the transient heat conduction theory, Qian et al. obtained the mechanical response and deformation effect of steel box girder by using different paving temperatures and paving thicknesses of the asphalt concrete, and demonstrated the influence of temperature field on the overall structure and pavement parameters of the bridge [12, 13]. Deng et al. applied the damage mechanics theory to study the fatigue damage of the pavement structure of bridge deck caused by sustained high temperature, and demonstrated that the damage of temperature to the pavement structure of bridge deck cannot be ignored [14]. Zhu et al. analyzed the dynamic response of single rear axle, double rear axles and three rear axles to the bridge under moving loads [15].

With the continuous development of urban three-dimensional transportation system, the application of viaducts is more and more extensive. Although the urban viaduct traffic system is conducive to relieving traffic pressure, the environmental vibration caused by it and the long-term stability of its own structure is becoming increasingly serious [16]. Siringoringo & Fujino found that the characteristics of wavelet can effectively characterize the state of isolation supports directly from the seismic responses of bridge [17]. To study the vibration control of multi-span beam bridge under the excitation of pier foundation, Bouna et al. combined the modal superposition method with the numerical analysis to predict the vibration response of the bridge under the excitation of the pier foundation [18]. Ma et al. selected 15 multi-span continuous girder bridges for vehicle-bridge coupling analysis. They studied the variation law of the dynamic amplification factor (DAF) of continuous girder bridge and found that the vehicle-bridge resonance was closely related to vehicle frequency, bridge frequency and interference frequency caused by vehicle motion, when the resonance occurs, DAF of the continuous girder bridge increases significantly [19, 20]. These researches on vehicle bridge coupling mostly used vertical force as the bridge deck force, and the pavement structure of bridge deck was mostly treated as dead load, but the properties of the pavement structure of bridge deck were not considered, and lacked of research on the changes of the stress and displacement of pavement layers under vehicle load.

In this study, a numerical model of three span continuous beam bridge was established and the dynamic response of the pavement layers of the bridge was solved by using the central difference method. The variation law of the vertical deflection, transverse stress and longitudinal stress the pavement layer, and the longitudinal beam under the vehicle load was revealed, which could provide the reference for the design of bridge deck [21, 23].

The rest of this study is organized as follows. Section 3 describes the relevant background and the research methods.

Section 4 gives the results and discussion, and finally, the conclusions are summarized in Section 5.

3. Methodology

3.1 Numerical calculation model

3.1.1 Steel-concrete composite beam model
A three span steel-concrete composite continuous beam model was established by using Abaqus software, as shown in Fig. 1. The specific size of the bridge came from an expressway, the continuous beam was 90 m long and 11.88 m wide. The longitudinal beam was composed of 4 I-beams, the height of I-beams was 1.65 m, and the spacing was 3.5 m. The short beams were used to connect the longitudinal beam, the spacing of short beams was 5 m, and the steel plate and beam were made of Q345D steel. The paving system of bridge deck was divided into the upper layer, the lower layer and the concrete layer. The concrete parameters of the bridge deck are shown in Table 1.
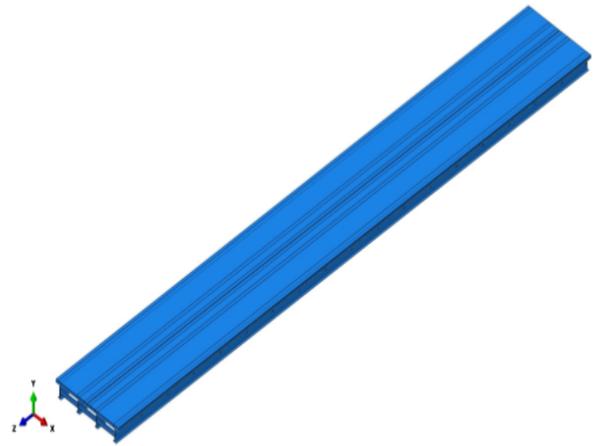

Fig. 1. Three-span continuous beam model.

The creep model is adopted for the upper layer and lower layer of the bituminous mixture, and the total strain $\varepsilon(t)$ of bituminous mixture under vehicle loads:

$$\varepsilon(t) = \varepsilon_e + \varepsilon_p + \varepsilon_c \tag{1}$$

where, ε_e is the elastic strain, ε_d is the plastic strain, ε_c is the creep strain.

Assuming the asphalt pavement does not reach the yielding state under the vehicle load, then $\varepsilon_d = 0$, the total strain is:

$$\varepsilon(t) = \varepsilon_e + \varepsilon_c \tag{2}$$

At the constant temperature, ε_c is the function of time and stress:

$$\varepsilon_c = f(t, \sigma) = \frac{A}{m+1} \sigma^n t^{m+1} \tag{3}$$

Table 1. Basic parameters of steel-concrete continuous beam model structure.

Structure of bridge	Thickness (mm)	E (MPa)	Poisson's ratio	Density (kg·m⁻³)	A	m	n
Upper layer (SMA-13)	40	1400	0.35	2400	1.464e-5	0.336	-0.502
Lower layer (AC-20)	60	1200	0.20	2300	4.802e-6	0.595	-0.532
Concrete surface layer	250	2.95e5	0.20	2300	—	—	—
Steel plate	15	2.10e5	0.30	7800	—	—	—
Top slab of beam	20	2.10e5	0.30	7800	—	—	—
Bottom slab of beam	25	2.10e5	0.30	7800	—	—	—

The strain rate of creep is $d\varepsilon_c / dt = A\sigma^n t^m$, which is generally applied to the constant load creep. For non-constant load creep, the time-independent creep strain rate is adopted:

$$\frac{d\varepsilon_c}{dt} = \left\{A\sigma^n[(m+1)\varepsilon_c]^m\right\}^{\frac{1}{m+1}} \quad (4)$$

Therefore, the time-independent creep strain rate was used to describe the mechanical behavior of bituminous mixture, and the linear elastic was used for other pavement materials.

$$Z_1 = Z_c - l_1\beta_c - d_{r2}\phi_c \quad (5)$$

$$Z_2 = Z_c + l_2\beta_c - d_{r2}\phi_c \quad (6)$$

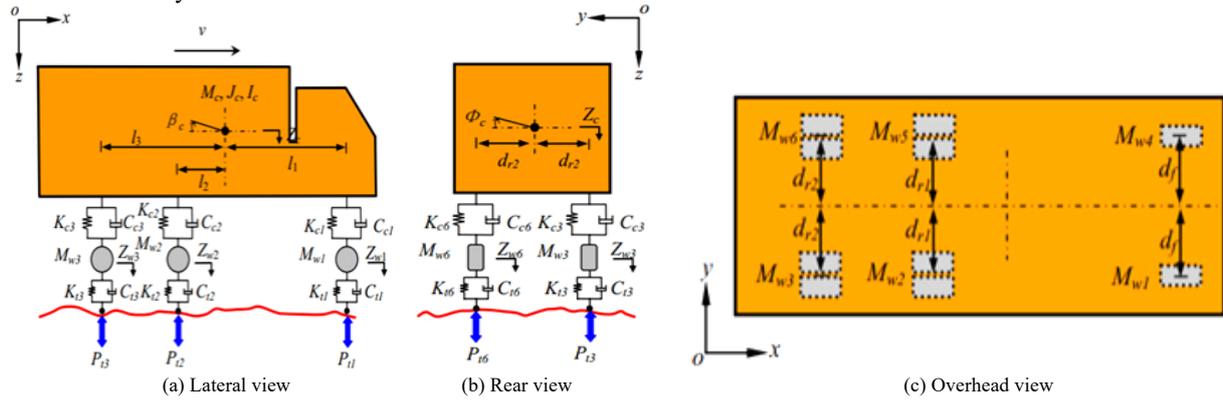$$Z_3 = Z_c + l_3\beta_c - d_{r2}\phi_c \quad (7)$$

$$Z_4 = Z_c - l_1\beta_c + d_{r2}\phi_c \quad (8)$$

$$Z_5 = Z_c + l_2\beta_c + d_{r2}\phi_c \quad (9)$$

$$Z_6 = Z_c + l_3\beta_c + d_{r2}\phi_c \quad (10)$$

3.1.2 Vehicle model
As shown in Fig. 2, due to the action of pitch angle β_c and roll angle ϕ_c, the vertical displacement of the suspension ends of the car body:

(a) Lateral view   (b) Rear view   (c) Overhead view

Fig. 2. Three-axis heavy-duty vehicle model.

Equation of vertical motion of the car body:

$$M_c\ddot{Z}_c = K_{c1}(Z_1 - Z_{w1}) + C_{c1}(\dot{Z}_1 - \dot{Z}_{w1}) + K_{c4}(Z_4 - Z_{w4}) + C_{c4}(\dot{Z}_4 - \dot{Z}_{w4}) + K_{c2}(Z_2 - Z_{w2})$$
$$+ C_{c2}(\dot{Z}_2 - \dot{Z}_{w2}) + K_{c5}(Z_5 - Z_{w5}) + C_{c5}(\dot{Z}_5 - \dot{Z}_{w5}) + K_{c3}(Z_3 - Z_{w3}) + C_{c3}(\dot{Z}_3 - \dot{Z}_{w3}) + K_{c6}(Z_6 - Z_{w6}) + C_{c6}(\dot{Z}_6 - \dot{Z}_{w6}) \quad (11)$$

Equation of pitch motion of the car body:

$$J_c\ddot{\beta}_c = l_1[K_{c1}(Z_1 - Z_{w1}) + C_{c1}(\dot{Z}_1 - \dot{Z}_{w1}) + K_{c4}(Z_4 - Z_{w4}) + C_{c4}(\dot{Z}_4 - \dot{Z}_{w4})] - l_2[K_{c2}(Z_2 - Z_{w2})$$
$$+ C_{c2}(\dot{Z}_2 - \dot{Z}_{w2}) + K_{c5}(Z_5 - Z_{w5}) + C_{c5}(\dot{Z}_5 - \dot{Z}_{w5})] - l_3[K_{c3}(Z_3 - Z_{w3}) + C_{c3}(\dot{Z}_3 - \dot{Z}_{w3}) + K_{c6}(Z_6 - Z_{w6}) + C_{c6}(\dot{Z}_6 - \dot{Z}_{w6})] \quad (12)$$

Equation of rolling motion of the car body:

$$I_c\ddot{\phi}_c = d_{r2}[K_{c1}(Z_1 - Z_{w1}) + C_{c1}(\dot{Z}_1 - \dot{Z}_{w1}) - K_{c4}(Z_4 - Z_{w4}) - C_{c4}(\dot{Z}_4 - \dot{Z}_{w4})] + d_{r2}[K_{c2}(Z_2 - Z_{w2}) + C_{c2}(\dot{Z}_2 - \dot{Z}_{w2})$$
$$- K_{c5}(Z_5 - Z_{w5}) - C_{c5}(\dot{Z}_5 - \dot{Z}_{w5})] + d_{r2}[K_{c3}(Z_3 - Z_{w3}) + C_{c3}(\dot{Z}_3 - \dot{Z}_{w3}) - K_{c6}(Z_6 - Z_{w6}) - C_{c6}(\dot{Z}_6 - \dot{Z}_{w6})] \quad (13)$$

Equation of vertical motion of the tire:

$$M_{w1}\ddot{Z}_{w1} = K_{t1}(Z_{w1} - P_{t1}) + C_{t1}(\dot{Z}_{w1} - \dot{P}_{t1}) - K_{c1}(Z_1 - Z_{w1}) - C_{c1}(\dot{Z}_1 - \dot{Z}_{w1}) \quad (14)$$

$$M_{w2}\ddot{Z}_{w2} = K_{t2}(Z_{w2} - P_{t2}) + C_{t2}(\dot{Z}_{w2} - \dot{P}_{t2}) - K_{c2}(Z_2 - Z_{w2}) - C_{c2}(\dot{Z}_2 - \dot{Z}_{w2}) \tag{15}$$

$$M_{w3}\ddot{Z}_{w3} = K_{t3}(Z_{w3} - P_{t3}) + C_{t3}(\dot{Z}_{w3} - \dot{P}_{t3}) - K_{c3}(Z_3 - Z_{w3}) - C_{c3}(\dot{Z}_3 - \dot{Z}_{w3}) \tag{16}$$

$$M_{w4}\ddot{Z}_{w4} = K_{t4}(Z_{w4} - P_{t4}) + C_{t4}(\dot{Z}_{w4} - \dot{P}_{t4}) - K_{c4}(Z_4 - Z_{w4}) - C_{c4}(\dot{Z}_4 - \dot{Z}_{w4}) \tag{17}$$

$$M_{w5}\ddot{Z}_{w5} = K_{t5}(Z_{w5} - P_{t5}) + C_{t5}(\dot{Z}_{w5} - \dot{P}_{t5}) - K_{c5}(Z_5 - Z_{w5}) - C_{c5}(\dot{Z}_5 - \dot{Z}_{w5}) \tag{18}$$

$$M_{w6}\ddot{Z}_{w6} = K_{t6}(Z_{w6} - P_{t6}) + C_{t6}(\dot{Z}_{w6} - \dot{P}_{t6}) - K_{c6}(Z_6 - Z_{w6}) - C_{c6}(\dot{Z}_6 - \dot{Z}_{w6}) \tag{19}$$

The matrix form of the above equation can be expressed:

$$M_q\ddot{u}_q(t) + C_q\dot{u}_q(t) + K_qu_q(t) = F_q(t) \tag{20}$$

where, M_q, C_q, K_q, $F_q(t)$ is the vibration mass matrix, damping matrix, stiffness matrix and external excitation matrix of vehicle, respectively. $\ddot{u}_q(t)$、$\dot{u}_q(t)$、$u_q(t)$ is vibration accelerator, velocity and displacement of vehicle, respectively.

Table. 2. Three-axle truck model parameters (HJG Automobile)

Model parameters	Value
Full load vehicle weight M_c/(t)	51.8
Full load front axle load M_a/(t)	10.8
Full load rear tandem axle load M_b/(t)	41
Stiffness of suspension spring of front axle K_{ci} (N/m)	243600
Stiffness of suspension springof rear axle K_c (N/m)	2178237
Suspension damping of front axle C_{ci} (N·s/m)	2420
Suspension damping of rear axle C_{ci} (N·s/m)	8500
Tire stiffness of front axle k_{ti} (N/m)	1100000
Tire stiffness of rear axle k_t (N/m)	2200000
Tire damping of front axle C_{ti} (N·s/m)	3500
Tire damping of rear axle C_{ti} (N·s/m)	11658
Vehicle pitch moment of inertia J_c (kg·m^{-2})	71540
Vehicle roll moment of inertia I_c (kg·m^{-2})	8920
Mass of the front wheel M_{w1} and M_{w4} (kg)	297
Mass of the rear wheel M_{w2}, M_{w3}, M_{w5}, and M_{w6} (kg)	460

According to the relationship between the contact point of the vehicle and the pavement, the force between the wheel and the pavement can be obtained:

$$R_t = W_i + K_{ti}(Z_{wi} - P_{ti}) + C_{ti}(\dot{Z}_{wi} - \dot{P}_{ti}) \tag{21}$$

where, W_i is the sum of car body weigth and its self-weight assigned to wheel i, when the vehicle is stationary.

To study the force of suspension, extracting the suspension force:

$$T_t = W_j + K_{ci}(Z_i - Z_{wi}) + C_{ci}(\dot{Z}_i - \dot{Z}_{wi}) \tag{22}$$

where, W_i is the weight of car body assigned to suspension.

In this study, a typical three axle vehicle model was adopted, and the relevant parameters of the vehicle model are shown in Table 2. Before numerical analysis, the initial displacement, velocity and acceleration of the vehicle were assumed to be zero.

3.1.3 Tire mode
In previous studies, some scholars assumed that the tire was a linear elastic body, that is, the suspension and tire were composed of mass block m, vertical stiffness k, and damping c. To make the vibration characteristics of the pavement

system of the steel-concrete composite beam bridge closer to the engineering practice, a simplified model of 12.00R20 radial tire was established, as shown in Fig. 3. Assuming that the materials of all parts of the tire are the same, the tire size: the height of section is 305.5 mm, the width of section is 310 mm, the diameter of tire is 1127 mm, the diameter of rim is 516 mm, and applying 0.7 MPa standard air pressure to the tire. In addition, rubber belongs to ultra-high elasticity material, its mechanics properties are very complex, with geometric and material double nonlinear. This kind of material can be expressed by volume strain energy, the constitutive equations of isotropy incompressible materials are as follows:

$$\sigma' = -p'I + \alpha_1 B + \alpha_2 B.B \tag{23}$$

$$\alpha_1 = 2\left(\frac{\partial U}{\partial I_1^B} + I_1^B\frac{\partial U}{\partial I_2^B}\right) \tag{24}$$

$$\alpha_2 = -2\frac{\partial U}{\partial I_2^B} \tag{25}$$

$$U = U(I_1^B, I_2^B) \tag{26}$$

where, σ' is the stress tensor of Cauchy material, p' is the hydrostatic pressure, U is the strain energy function, B is the deformation tensor of Cauchy material, and I_1^B and I_2^B are first and second invariants.

It is found that the contribution of parameter I_2^B in the strain energy is very small and can be ignored, then the strain energy function can be simplified as:

$$U = C_{10}\left(I_1^B - 3\right) + C_{20}\left(I_1^B - 3\right)^2 + C_{30}\left(I_1^B - 3\right)^3 \tag{27}$$

Parameters C_{10}, C_{20}, C_{30} can be determined by static uniaxial compression and tensile tests, and those test parameters can better simulate the mechanical behavior of the tire under complex conditions.

The curtain layer-rubber is generally simulated with embedded reinforcement bars, in which the curtain layer takes the surface element as the basic unit and the reinforcement adopts Rebar unit, as shown in Fig. 3. The rebar element type was defined according to the curtain layer geometry, and then the surface element was implanted into the rubber solid element [24, 25]. In addition, the rubber material adopts CGAX4H and CGAX3H unit types, and the curtain layer adopts SFMGAX1 unit types. The mechanical parameters of tire are shown in Table 3.
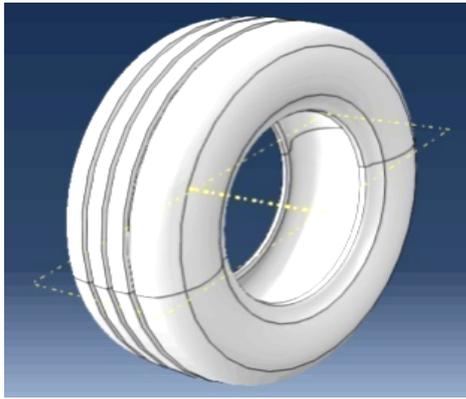
Fig. 3. The model of tire.

Table 3. Mechanical parameters of tire.

Composition	E (MPa)	v	ρ (kg.m^{-3})	C10 (MPa)	C20 (MPa)	C30 (MPa)
Rubber	-	-	1025	6.0	6.0	6.0
Metal tyre	3428.5	0.45	1200	-	-	-
Tire bead	2.10e5	0.30	7800	-	-	-

3.1.4 Tire-deck coupling model

The tire and steel-concrete continuous beam bridge coupling model consists of two parts: tires and three span continuous beam bridge, as shown in Fig. 4. The two components are connected by the contact of tire and the bridge deck, the dynamic equation of the tire-bridge coupling system is:

$$\begin{bmatrix} M_{vv} & 0 \\ 0 & M_{rr} \end{bmatrix}\begin{Bmatrix} \ddot{Y}_v(t) \\ \ddot{Y}_b(t) \end{Bmatrix} + \begin{bmatrix} C_{vv} & C_{vr} \\ C_{rv} & C_{rr} \end{bmatrix}\begin{Bmatrix} \ddot{Y}_v(t) \\ \ddot{Y}_r(t) \end{Bmatrix} + \begin{bmatrix} K_{vv} & K_{vr} \\ K_{rv} & K_{rr} \end{bmatrix}\begin{Bmatrix} Y_v(t) \\ Y_r(t) \end{Bmatrix} + \begin{Bmatrix} R_v \\ R_r \end{Bmatrix} = \begin{Bmatrix} P_{vr}(t) \\ P_{rv}(t) \end{Bmatrix} \quad (28)$$

where, M, C, K are the mass, damping and elastic stiffness matrices, respectively. $\ddot{Y}$, $\dot{Y}$, Y are the acceleration, velocity and displacement vectors, respectively. The subscripts v and r represent bridge and tire, respectively. R_v is the restoring force of wheel, R_r is the restoring force of bridge, P_{vr}, P_{rv} are the force between the wheel and the bridge.

Fig. 4. The coupling model of tire and continuous beam.

It can be seen from Eq. (28) that the matrix equation is a second order nonlinear differential equation, which can be solved by the central difference methods.

To synchronize the rotation of the two tires, Hinge connection unit is used to connect the axis of tires. Two tires rotate around the wheel center at the same time, and the suspension force is applied to the middle part of the wheel spindles, as shown in Fig. 5. In addition, applying a horizontal speed to the wheel spindle, set a certain friction coefficient μ on the bridge deck, and then tires keep rolling forward under the effect of friction.
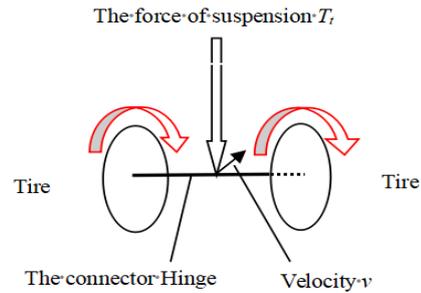

Fig. 5. Tire rotation of tires.

3.2 Boundary conditions and contact modes

The first span tail of the continuous beam bridge is constrained in the x, y and z directions, and the rest parts are constrained in the x and y directions. In addition, the tires are constrained in the x direction, and the rotation constraint is applied on the yz plane.

The surface to surface contact is adopted between the tire and the continuous beam, which includes the normal contact and tangential contact. Wherein, "hard contact" is adopted for normal contact, and the penalty function is adopted for normal force:

$$f_n = \begin{cases} k_n C & C \geq 0 \\ 0 & C < 0 \end{cases} \quad (29)$$

where, k_n is the normal contact stiffness, C is the gap value, which is determined by the position of the contact node and the target plane.

Tangential contact mainly considers the motion state between contact surfaces, and the small sliding is allowed on contact surfaces. In addition, the friction between contact surfaces should be considered:

$$f_s = \begin{cases} k_t n^e & (\text{No sliding}) \\ \mu f_n & (\text{Slding}) \end{cases} \quad (30)$$

where, k_t is the shear stiffness, n^e is the elastic deformation of the contact node relative to the target plane, μ is friction coefficient.

3.3 Roughness analysis of the bridge deck pavement

In the vehicle bridge coupling analysis, the introduction of the roughness of the bridge deck can improve the accuracy of the calculation results, and accord more perfectly with the engineering practice. In this paper, the power spectral density of road $G_q(n_0)$ in the Chinese standard GB/T7031-86 (Expression Method of Vehicle Vibration Input Road Roughness) is used to express the bridge deck roughness:

$$G_q(n) = G_q(n_0)\left(\frac{n}{n_0}\right)^{-w} \quad (31)$$

where, n is the spatial frequency, (m^{-1}), n_0 is the frequency of reference spatial, takes n_0=0.1 m^{-1}, $G_q(n_0)$ is the coefficient of road roughness, w is the frequency index, takes w=2.

The random phase cosine superposition method is adopted for road roughness:

$$r(x) = \sum_{i=1}^{N} \sqrt{4G(n_i)\Delta n} \cos(n_i x + \theta_i) \qquad (32)$$
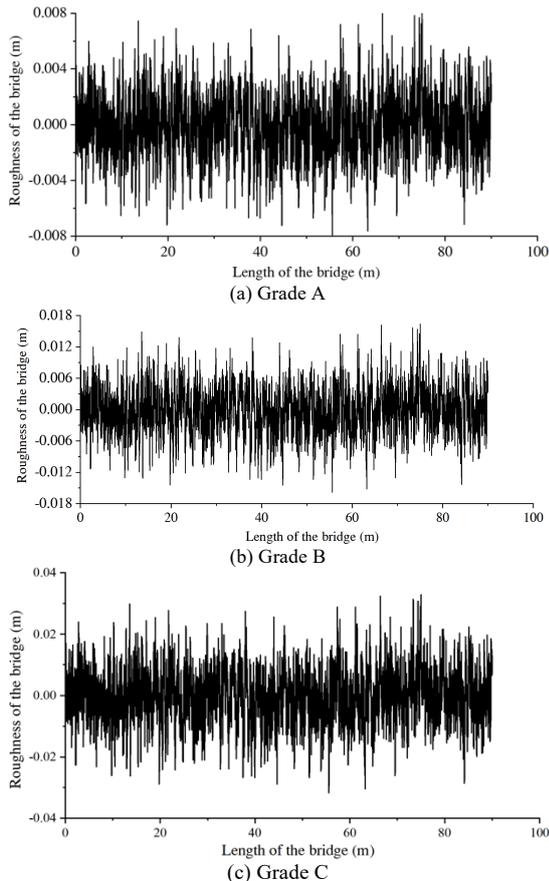
where, $r(x)$ is the bridge deck roughness, x is the longitudinal position of the bridge deck, $G(n_i)$ is the the power spectral density function, n_i is the spatial frequency, Δn is the increment of frequency, θ_i is the random phase angle in $[0, 2\pi]$

According to the Chinese standard GB/T7031-8, the road roughness is divided into eight grades by the power spectral density. The lower limit, upper limit and geometric average of the grade coefficient of road roughness are shown in Table 4.

Table 4. The roughness coefficient of the bridge deck.

Road level	The roughness coefficient of the bridge deck $G_q(n_0)$ $(10^{-6}m^2/m^{-1})$		
	Lower limit	Geometric average	Upper limit
A	8	16	32
B	32	64	128
C	128	256	512
D	512	1024	2048
E	2048	4096	8192
F	8192	16384	32768
G	32768	65536	131072
H	131072	262144	524288

According to the roughness coefficient of the bridge deck, MATLAB/SIMULINK were used to obtain the curve of different roughness levels, as shown in Fig. 6.

(a) Grade A

(b) Grade B

(c) Grade C

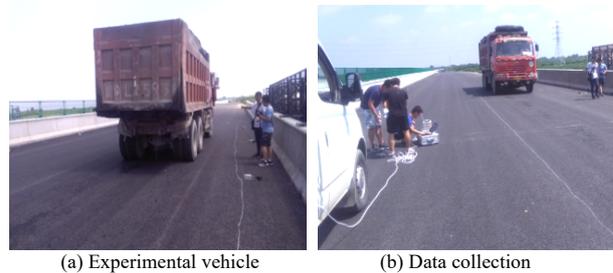**Fig. 6.** The grade spectrum of bridge deck roughness.

It is found that the actual roughness of bridge deck is similar to grade B road roughness by the test of the laser pavement smoothness instrument, so the grade B roughness coefficient is used in model verification.

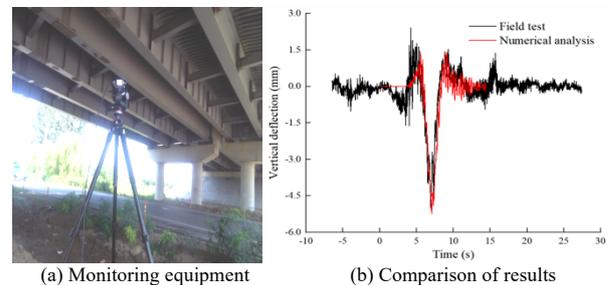## 4. Results analysis and discussion

4.1. Model validation analysis

To verify the correctness of the simulation results of the three span steel-concrete composite continuous beam bridge, a three axle Hongyan Diamond truck with a load of 50 t passes through the three span steel-concrete composite continuous beam bridge at a constant speed, as shown in Fig. 7. The IMETRUM non-contact video measuring instrument was used to measure the middle part of the continuous beam bridge, and the field monitoring results and numerical calculation results are shown in Fig 8. The experimental value and simulation calculation value of the vertical deflection of the second span are shown in Table 5, and the test values and simulation calculation values of the frequency of the continuous beams are shown in Table 6.

From the comparison between field test and numerical analysis, it can be seen that the difference between field test and numerical analysis results is within 10%, which verifies the accuracy of the results of the numerical simulation.

(a) Experimental vehicle   (b) Data collection
Fig. 7. Field test.

(a) Monitoring equipment   (b) Comparison of results
Fig. 8. Comparison of results with speed of 50 km/h.

Table 5. Vertical deflection of the second span.

Velocity (km/h)	Field test (mm)	Numerical calculation (mm)	Error (%)
25	5.30	5.78	9.10
40	4.89	5.20	6.30
50	4.99	5.30	6.20

Table 6. The frequency of continuous beams.

Mode	Field test (Hz)	Numerical calculatio (Hz)	Error (%)
First mode	3.516	3.345	4.80
Second mode	4.102	4.173	1.70
Third mode	4.980	5.256	7.50

4.2 Deflection response of the continuous beam

4.2.1 Mid-span deflection of beam under different loads

It can be seen from Fig. 9, the variation lawof the deflection at the mid-span of continuous beam is similar and distributed symmetrically under the interaction of the linear elastic load and tire load. In addition, the peak value of vertical deflection caused by the suspension force of tires is 1.12 mm,

and the peak value of vertical deflection caused by the bridge deck contact force is 1.04 mm, with an error of 7.7%.
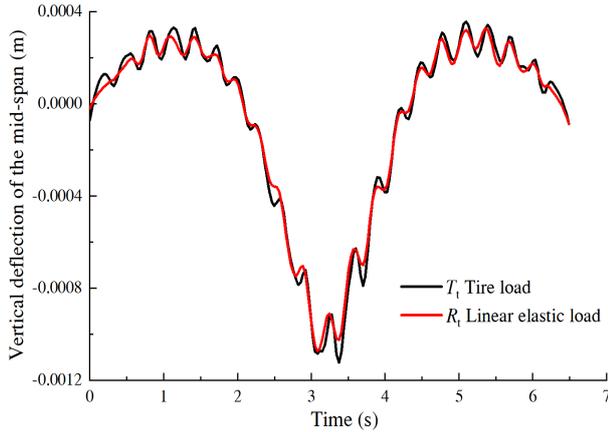

Fig. 9. Vertical deflection variation of bridge under different loads.

It can be seen from Fig. 10, the maximum vertical deflection of the mid-span under the grade A, B and C roughness is 0.995 mm, 1.12 mm and 1.16 mm, respectively. The maximum deflection of grade B and C roughness is greater than 12.7% and 16.6% of that of grade A. The higher the grade of deck roughness, the greater the vertical deflection of the mid-span of the bridge. In addition, compared with grade B and C roughness, the deflection curve of the bridge deck under grade A roughness is smoother, while the deflection curve of the bridge deck under grade B and C roughness is more violent. This shows that the dynamic response of the bridge deck is relatively large under grade C roughness.

4.2.2 Bridge deck deflection at different driving speeds
As seen from Fig. 11, when the vehicle speed is 50 km/h, 60 km/h and 80 km/h, the corresponding maximum deflections of the bridge deck are 1.12 mm, 1.01 mm and 0.857 mm respectively. To sum up, the higher the vehicle speed, the smaller the vertical deflection of the bridge deck.
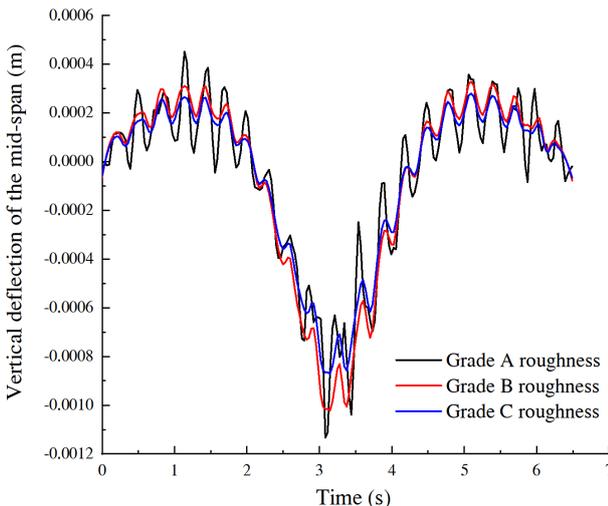

Fig. 10. Vertical deflection variation of bridge under different grades of roughness.
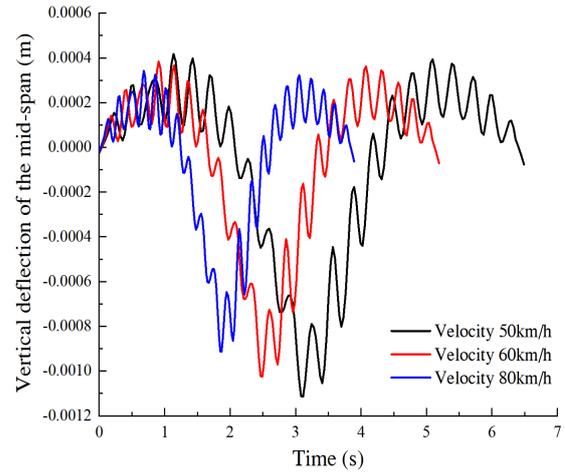

Fig. 11. The vertical deflection variation of the bridge deck under different driving speeds.

4.2.3 Bridge deck deflection under different axle loads
It can be seen from Fig. 12, the vertical deflection of the bridge deck with different vehicle axle loads varies greatly. When the axle load is 20 t, 35 t and 50 t, the maximum vertical deflection of bridge is 0.49 mm, 0.71 mm and 1.12 mm, respectively. Compared with the 50 t axle load, the deflection of bridge deck of 35 t and 20 t axle loads decreased by 36.6% and 56.3%, respectively. The greater the axle load, the greater the vertical deflection of the bridge deck, and the vehicle axle load is a crucial factor for the stability of the bridge deck.
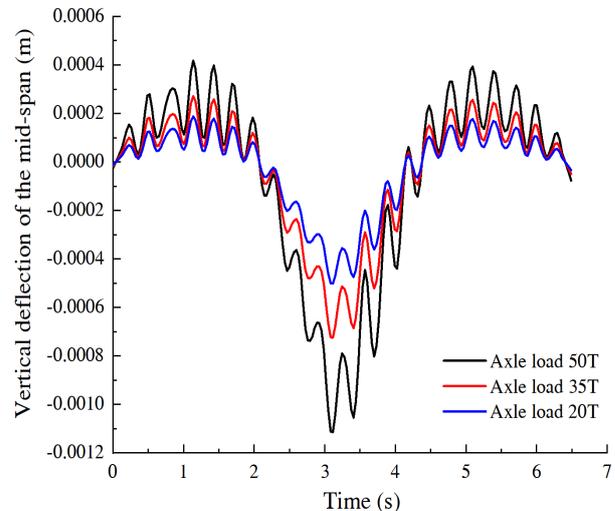

Fig. 12. The vertical deflection variation of bridge deck under different axle loads.

4.2.4 Deflection analysis of pavement layers of the bridge
IAs seen from Fig. 13, the vertical deflection variation law of the pavement layers is similar and the difference between the values is small, and shows a symmetrical distribution. The maximum vertical deflection of the pavement layers is about 1.12 mm, the maximum vertical deflection of the bottom of the main longitudinal beam is 1.02 mm, and the vertical deflection of the main longitudinal beam is 8.9% smaller than that of the pavement layers. To sum up: the deflection of the pavement layers of the steel concrete continuous beam is greater than that of the main longitudinal beam.
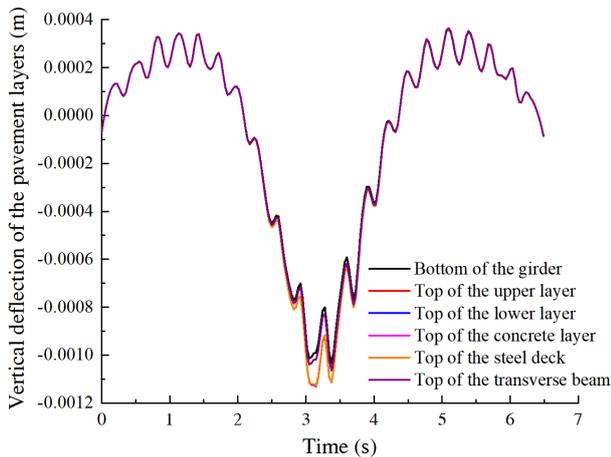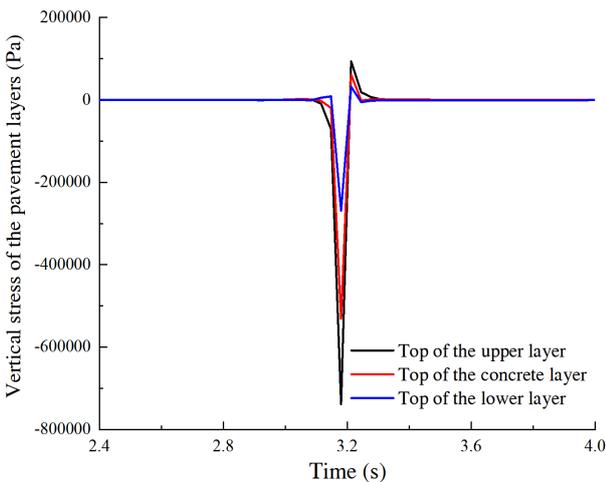
Fig. 13. The vertical deflection variation of the pavement layers.

(c) The bottom of the longitudinal beam

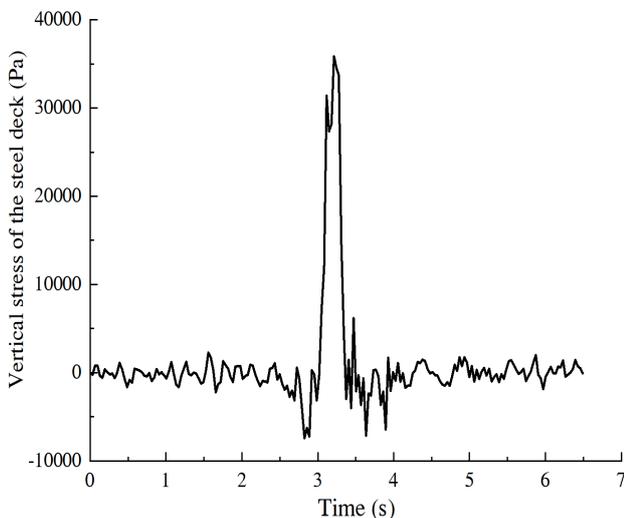**Fig.14.** Time history curve of vertical stress of the bridge.

4.3. Stress response analysis of the continuous beam

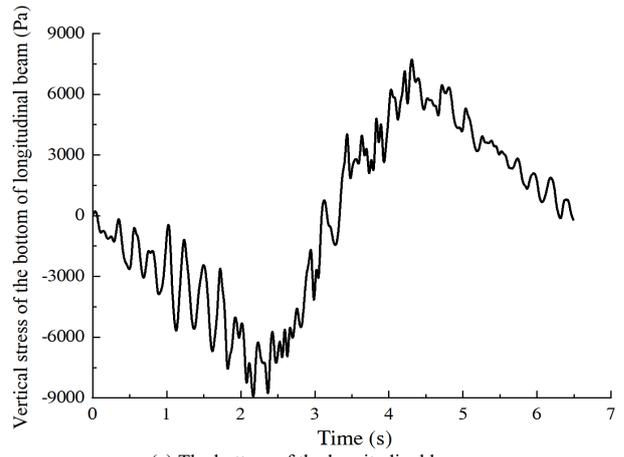#### 4.3.1 Vertical stress analysis of pavement layers

As seen from Fig. 14(a), the vertical stress of the upper layer of pavement is the largest, followed by the lower layer, and the concrete layer is the smallest. When the vehicle tires are about to leave observation points (3.2 s - 3.3 s), the vertical stress appears a temporary tensile state, and the maximum tensile stress is 0.09 MPa at the top of the upper layer. The phenomenon of tensile stress is closely related to the triaxial uneven contact force of the tires.

(a) The pavement layers of bridge
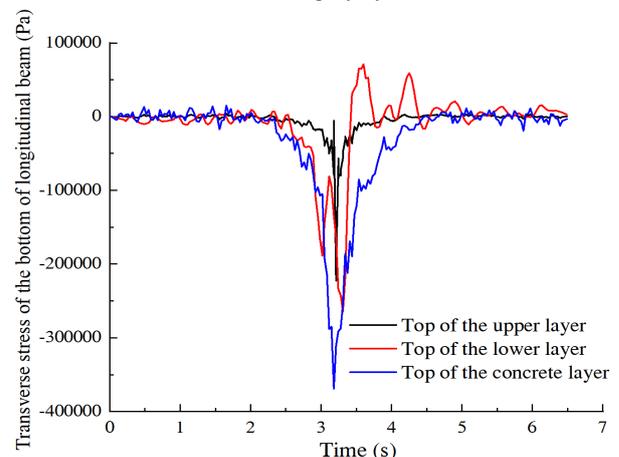

(b) The steel deck of bridge

As seen from Fig. 14(b), the steel panel of the bridge is in a tensile state, and the maximum stress value is 35000 Pa. Only when t=2.8 s and t=3.6 s, the steel panel of the bridge is in a transient state of compression, and the maximum stress is 750 Pa, which is roughly symmetrically distributed.

As seen from Fig. 14(c), the distribution of the vertical stress at the bottom of the I-beam is relatively complex. when t=0-3.25 s, the vertical stress of the longitudinal beam is in a compressed state, and its maximum value is 8800 Pa. When t=3.25 s-6.5 s, the vertical stress of the longitudinal beam is in a tensile state, and its maximum value is 7800 Pa.

4.3.2 Transverse stress analysis of the pavement layers

As seen from Fig. 15(a), the change characteristics of the lateral stress curve of the upper layer and the concrete layer are similar. When the tire is near the middle of the bridge, the transverse stress of the pavement layer gradually increases. When the tire drives away, the transverse stress of the pavement layer decreases gradually, the maximum transverse stress is 0.23 MPa at the the upper layer, and the maximum transverse stress is 0.378 MPa at the the concrect layer. In addition, the distribution of the transverse stress at the lower layer is relatively complex. When the tire is about to leave the middle of the bridge (3.5 s-4.2 s), the transverse stress of the lower layer is tensile stress, and the maximum value is 0.051 MPa.

It can be seen from Fig. 15(b), the transverse stress of the steel deck of bridge is tensile stress, the maximum value is 3.18 MPa, and the curve is roughly symmetrical distribution.
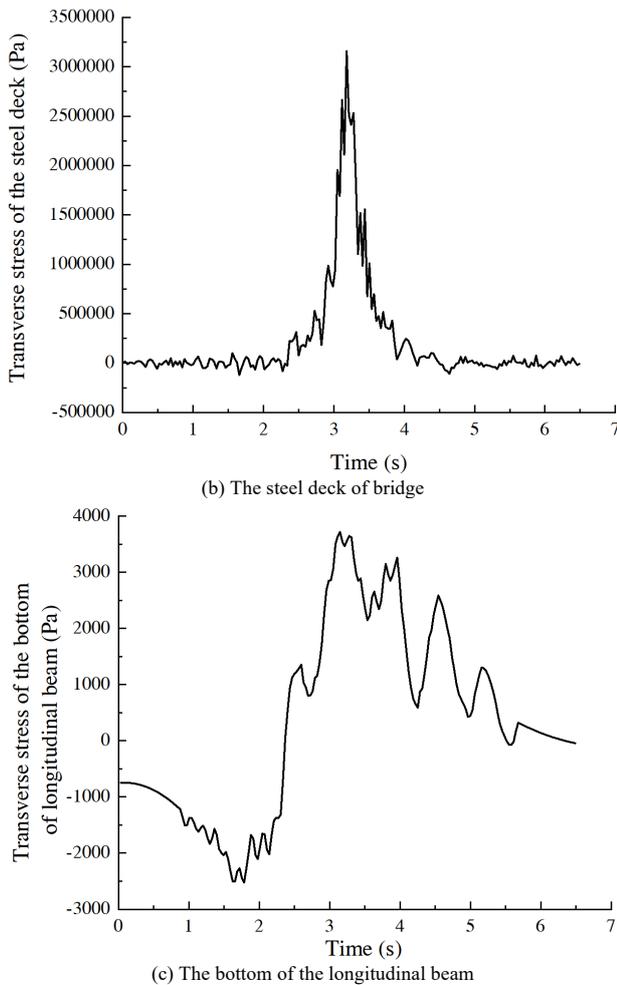

(a) The pavement layers of bridge

(b) The steel deck of bridge

(c) The bottom of the longitudinal beam

Fig. 15. Time history curve of transversal stress of bridge.

As seen from Fig. 15(c), the variation law of the transverse stress at the bottom of longitudinal beam is relatively complex. In the time period of *t*=0 s-3.25 s, the bottom of the longitudinal beam is in a compression state, and the maximum compressive stress is 2560 Pa. In the time period of *t*=3.25 s-6.5 s, the bottom of the longitudinal beam is in the state of tension, the maximum tensile stress is 3300 Pa, and the fluctuation of the stress is severe during the tension period.

4.3.3 Longitudinal stress analysis of the pavement layers
As seen from Fig. 16(a), the pavement layers of the bridge is in the state of tension in the time period *t*=0 s to 2.17 s. The tensile stress of the upper part of the concrete layer is the largest, followed by the lower layer, and the upper layer is the smallest. In the time period *t*=2.17 s-4.41 s, the stress of the pavement layers of the bridge is relatively complex, and the variation law of the longitudinal stress of the upper layer and the concrete layer is similar. In addition, with the increase of time, the longitudinal stress gradually increases, and then gradually decreases to 0 after reaching a certain value. Among of them, the maximum longitudinal compressive stress of the concrete layer is 0.286 MPa, the maximum longitudinal compressive stress of the upper layer is 0.21 MPa. The variation law of the longitudinal stress of the lower layer is relatively complex, and at the beginning the lower layer is in a state of tension, when the wheel passes the observation point, it is in the compression state. In the period of *t*=4.41 s-6.50 s, the longitudinal stress of the

pavement layers of the bridge is similar to that in the period of *t*=0 s-2.17 s.

As seen from Fig. 16(b), the longitudinal stress of the steel deck of the bridge is in the tensile state, and the maximum tensile stress is 2.18 MPa. Among them, in the early stage of loading *t*=0 s-3 s, the fluctuation of longitudinal stress of the steel deck is relatively small, and in the late stage of loading *t*=3.4 s-6.5 s, the fluctuation of the longitudinal stress of the steel deck is relatively large.

(a) The pavement layers of bridge

(b) The steel deck of bridge

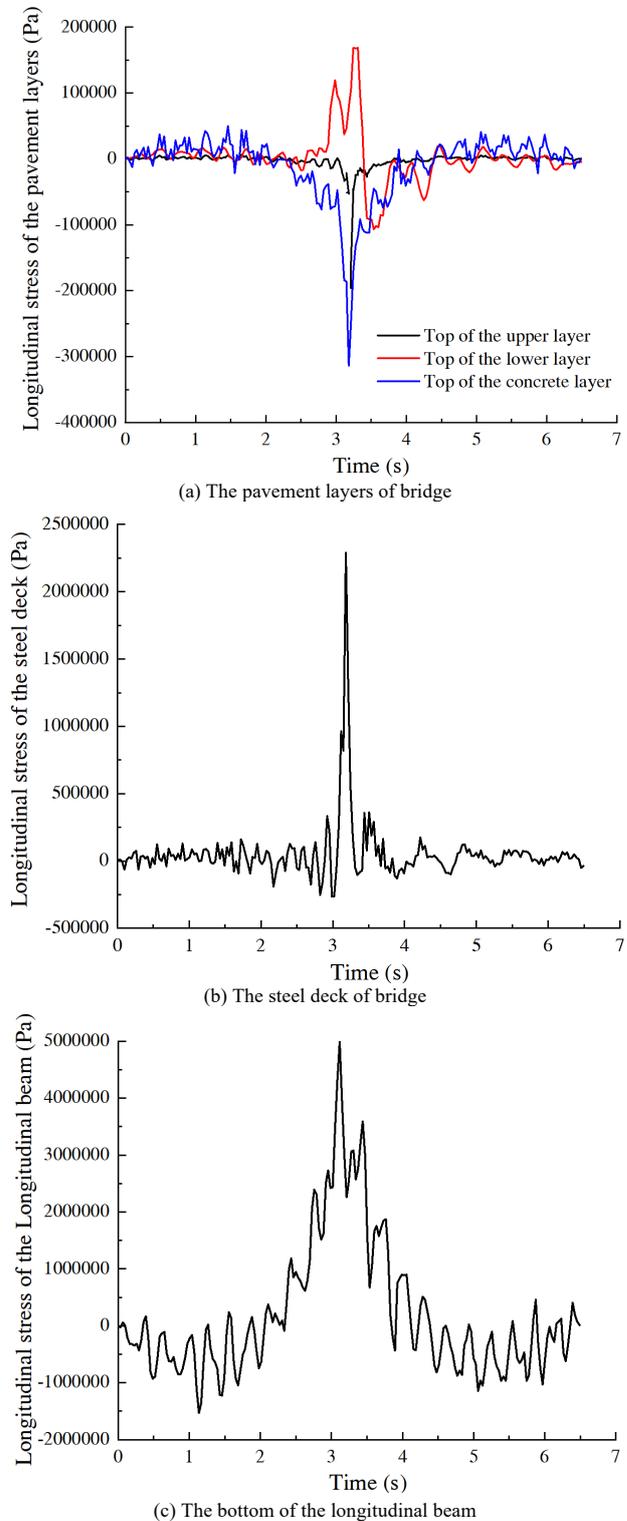(c) The bottom of the longitudinal beam

Fig. 16. Time history curve of longitudinal stress of bridge.

It can be seen from Fig. 16(c), the bottom of the I-beam is in the state of tension in the time period *t*=0 s-2.17 s, and the maximum compressive stress is 1.15 MPa. the bottom of

the I-beam is in the state of tension in the time period t=2.17 s-4.41 s, and the maximum tensile stress is 4.67 MPa. In addition, in the period of t=4.41 s-6.50 s, the variation law of the longitudinal stress is similar to that in the period of t=0 s-2.17 s.

5. Conclusions

In this study, a multi degree of freedom vehicle model was established, the suspension force of rear axle and the contact force of the bridge were extracted, and the suspension force was applied to the middle of the tire, compared with the contact force directly acting on the bridge deck, the main conclusions are as follows:

(1) The vertical deflection of the pavement layers of the continuous beam bridge under the triaxial force of tire is greater than that generated by the contact force of bridge deck, with a difference of about 7.7%. Under the triaxial force of tire, the vertical deflection difference of the upper layer, the lower layer, the concrete layer and the steel deck bridge is very small, while the vertical deflection of the bottom of the I-beam is 8.9% smaller than that of the pavement layers of the bridge deck.

(2) The vertical stress of the steel deck is in the state of tension, while the vertical stress of the bottom of the I-beam is in the state of compression at the early stage, and in the state of tension at the late stage. Under the triaxial force of tire, the vertical stress of the upper layer, the lower layer and the concrete layer are in the state of compression. When the vehicle is about to leave, the lower layer appears intermittent tensile stress, the transverse stress of the steel deck of the bridge is in the compression state.

(3) Under the triaxial force of tire, the variation characteristics of the longitudinal stress of the upper layer and the concrete layer is similar. The transverse stress of the lower layer appears the tension-compression alternate phenomenon, and the longitudinal stress of the steel deck of the bridge is in the tension state. The longitudinal stress of the bottom of the I-beam is symmetrically distributed, with tension in the middle and compression on both sides.

Although the dynamic response and mechanical characteristics of the steel-concrect continuous bridge under vehicle-bridge coupling were analyzed, in view of the complexity of vibration in vehicle-bridge coupling, the types and spans of viaducts will be further analyzed.

References

1. Ding, Y. L., Bian, Y., Zhao, H. W., Yue, Q., Wu, L. Y. "Long-term monitoring and analysis of vertical deflections of a highway-railway cable-stayed bridge under operation conditions". *Journal of Railway Science and Engineering*, 14(2), 2017, pp. 271-277.
2. Su, X. F., Fu, P., Ding, Z. J., Li, D. W., Yang, M. F. "Establishment and simulation analysis of tire finite element model based on abaqus software". *China Rubber Industry*, 66(2), 2019, pp. 121-127.
3. Yan, Z. Y., Chen, E. L., Zhen, W., Si, C. D. "Research on mesoscopic response of asphalt pavement structure under vibration load". *Shock and Vibration*, 2019, 2019, pp. 2620305.
4. Ali, V., Mohammad, S. R. "Investigating the effect of span-length and earthquake directivity on the response of multi-span continuous girder bridges isolated by friction bearings". *Bridge Structures*, 16(1), 2020, pp. 27-37.
5. Suangga, M., Haripriambodo, T. "Maximum deflection of three span continuous bridge using rotation data based on 3 dimensional model". *Earth and Environmental Science*, 794(1), 2021, pp.1-14.
6. Mizrak, C., Esen, I. "The optimisation of rail vehicle bogie parameters with the fuzzylogic method in order to improve passenger comfort during passage over bridges". *International Journal of Heavy Vehicle Systems*, 24(2), 2017, pp. 113-139.
7. Bayane, I., Pai, S. G. S., Smith, I. F. C., Brühwiler, E. "Model-based interpretation of measurements for fatigue evaluation of existing reinforced concrete bridges". *Journal of Bridge Engineering*, 26(8), 2021, pp. 1-10.
8. Narazaki, Y., Hoskere, V., Chowdhary, G., Spencer, B. F. "Vision-based navigation planning for autonomous post-earthquake inspection of reinforced concrete railway viaducts using unmanned aerial vehicles". *Automation in Construction*, 13(7), 2022, pp. 1-12.
9. Aloisio, A., Pasca, D. P., Battista, L. D., Rosso, M. M., Cucuzza, R., Marano, G. C., Alaggio, R. "Indirect assessment of concrete resistance from FE model updating and Young's modulus estimation of a multi-span PSC viaduct: Experimental tests and validation". *Structures*, 37, 2022, pp. 686-697.
10. Hou, Z. M., Xia, H., Zhang, Y. L., Wang, Y. "Analytical dynamic slip solution for steel concrete composite beams under harmonic load". *Journal of Vibration and Shock*, 35(2), 2016, pp. 18-23.
11. Li, H. L., Xia, H. "Fatigue reliability evaluation of steel bridges based on coupling random vibration analysis of train and bridge". *Engineering Mechanics*, 34(2), 2017, pp. 69-77.
12. Qian, Z. D., Hu, J., Liu, Y., Yang, Y. N. "Influence of gussasphalt concrete paving temperature on mechanical responses and deformation effects of steel box girder". *China Civil Engineering Journal*, 48(2), 2015, pp. 96-102.
13. Wang, Y., Wang, L. J., Lu, Y. J., Si, C. L. "Simulation on viscoelastic behavior of asphalt pavement under complex moving wheel load". *Journal of Vibration and Shock*, 36(15), 2017, pp. 181-186.
14. Deng, L., Duan, L. L., He, W., Ji, W. "Study on vehicle model for vehicle-bridge coupling vibration of highway bridges in china". *China Journal of Highway and Transport*, 31(7), 2018, pp. 92-100.
15. Zhu, Z. H., Wang, L. D., Gong, W., Yu, Z. W., Cai, C. B. "Study on vertical random vibration of train-bridge coupled system based on improved iteration model". *Journal of Hunan University(Natural Sciences)*, 43(11), 2016, pp. 120-130.
16. Wu, W. Q., Zhang, H., Liu, Z., Wang, Y. P. "Numerical analysis on transverse splicing structure for the widening of a long multi-span highway concrete continuous box girder bridge". *Materials*, 15(19), 2022, pp. 805-6805.
17. Siringoringo, D. M., Fujino, Y. "Wavelet-based analysis for detection of isolation bearing malfunction in a continuous multi-span girder bridge". *Journal of Earthquake Engineering*, 26(10), 2022, pp. 5237-5267.
18. Bouna, H. S., Nbendjo, B. R. N., Woafo, P. "Isolation performance of a quasi-zero stiffness isolator in vibration isolation of a multi-span continuous beam bridge under pier base vibrating excitation". *Nonlinear Dynamics*, 100, 2020, pp. 1-17.
19. Ma, L., Zhang, W., Han, W. S., Liu, J. X. "Determining the dynamic amplification factor of multi-span continuous box girder bridges in highways using vehicle-bridge interaction analyses". *Engineering Structures*, 181, 2019, pp. 47-59.
20. Stoura, Charikleia. D., Dimitrakopoulos, E. G. "A Modified bridge system method to characterize and decouple vehicle-bridge iinteraction". *ACTA Mechanica*, 231(9), 2020, pp. 3824-3845.
21. Wang, S. R., Shi, K. P., He, Y. S., Wang, X. Q. "Dynamic response analysis of middle pillar for ultra-small spacing tunnels under train

vibration loads". *Journal of Engineering Science and Technology Review*, 12(3), 2019, pp. 30-37.

22. Luo, T., Wang, S. R., Zhang, C. G., Liu, X. L. "Parameters deterioration rules of surrounding rock for deep tunnel excavation based on unloading effect ". *DYNA*, 92(6), 2017, pp. 648-654.

23. Wang, S. R., Shi, K. P., Zou, Y. F., Zou, Z. S., Wang, X. C., Li, C. L. "Size effect analysis of scale test model for high-speed railway foundation under dynamic loading condition". Tehnicki Vjesnik-Technical Gazette, 28(5), 2021, pp. 1615-1625.

24. Wang, S. R., Liu, Z. W., Qu, X. H., Fang, J. Bo. "Large deformation mechanics mechanism and rigid-gap-flexible-layer supporting technology of soft rock tunnel". *China Journal of Highway and Transport*, 22(6), 2009, pp. 90-95.

25. Pisačić, K., Horvat, M., Botak, Z. "Finite difference solution of plate bending using Wolfram Mathematica". *Technical Journal*, 13(3), 2019, pp. 241-247.